Diphosphine-induced chiral propeller arrangement of gold nanoclusters for singlet oxygen photogeneration

Jiangwei Zhang[1,§], Yang Zhou[1,2,§], Kai Zheng[1], Hadi Abroshan[3], Douglas R. Kauffman[4], Junliang Sun[5], and Gao Li[1]

Address correspondence to gaoli@dicp.ac.cn

[1]*State Key Laboratory of Catalysis, Dalian Institute of Chemical Physics, Chinese Academy of Sciences, Dalian 116023, China*

[2]*University of Chinese Academy of Sciences, Beijing 100049, China*

[3]*SUNCAT Center for Interface Science and Catalysis, Department of Chemical Engineering, Stanford University, 443 Via Ortega, Stanford, California 94305, USA*

[4]*National Energy Technology Laboratory (NETL), United States Department of Energy, Pittsburgh, Pennsylvania 15236, USA*

[5]*Beijing National Laboratory for Molecular Sciences, State Key Laboratory of Rare Earth Materials Chemistry and Applications, College of Chemistry and Molecular Engineering, Peking University, Beijing 100871, China* [§]*Jiangwei Zhang and Yang Zhou contributed equally to this work.*

ABSTRACT

In this study, 1,2-bis(diphenylphosphino)ethane (dppe) ligands are used to synthesize gold nanoclusters with an icosahedral Au_{13} core. The nanoclusters are characterized and formulated as $[Au_{13}(dppe)_5Cl_2]Cl_3$ using synchrotron radiation X-ray diffraction, UV/Vis absorption spectroscopy, electrospray ionization mass spectrometry, and density functional theory (DFT) calculations. The bidentate feature of dppe ligands and the positions of coordinating surface gold atoms induce a helical arrangement that forms a propeller-like structure, which reduces the symmetry of the gold nanocluster to C_1. Therefore, dppe ligands perform as a directing agent to create chiral an ansa metallamacrocycle $[Au_{13}(dppe)_5Cl_2]^{3+}$ nanocluster, as confirmed by simulated electronic circular dichroism spectrum. The highest occupied molecular orbital (HOMO)–lowest unoccupied molecular orbital (LUMO) gap of the $[Au_{13}(dppe)_5Cl_2]^{3+}$ cluster is determined as approx. 1.9 eV, and further confirmed by ultraviolet photoemission spectroscopy analysis and DFT simulation. Furthermore, the photoactivity of $[Au_{13}(dppe)_5Cl_2]^{3+}$ is investigated, with the nanocluster shown to possess near-infrared photoluminescence properties, which can be employed for $^1O_2$ photogeneration. The quantum yield of $^1O_2$ photogeneration using the $[Au_{13}(dppe)_5Cl_2]^{3+}$ nanocluster is up to 0.71, which is considerably higher than those of anthracene (an organic dye), and Au_{25} and Au_{38} nanoclusters.

1 Introduction

Metal nanoclusters containing 10–200 atoms are of great scientific interest as nanomaterials because they bridge the gap between discrete atoms and bulk metals [1, 2]. In particular, atomically precise gold nanoclusters are receiving increasing attention due to their applications in a wide range of disciplines, including catalysis, biology, and sensors [3–8]. Protecting Au clusters with organic ligands is an efficient strategy for synthesizing materials with exceptional stability and tunable properties [1, 2]. The use of phosphine ligands to protect gold nanoclusters when forming atomically precise gold nanoclusters can be traced back to 1970s [9]. Since then,

much effort has been focused toward the synthesis of gold nanoclusters protected by thiolate and phosphine ligands, ranging from ultra-small Au_4 to larger Au_{246} [1, 10–13]. Among the basic topological motifs of gold nanoclusters, icosahedral Au_{13} has received huge attention. This motif can widely be utilized as a synthon for the formation of larger clusters, such as Au_{38}, by fusion [11, 14], or smaller clusters, such as Au_{11}, by etching [15, 16].

Chirality plays an essential role in many fields, including chemistry, pharmacology, biology, and medicine. The synthesis of chiral nanomaterials provides an exciting opportunity for developing novel biomedical technologies and medicines. Chirality can often be induced in metal clusters through two methods: (i) designing intrinsically chiral metal cores; or (ii) using chiral organic ligands that cover the achiral core. However, achiral organic ligands arranged in a specific manner on a gold cluster surface can also cause the whole cluster to be chiral [17, 18].

For an ideal icosahedral Au_{13} kernel possessing high symmetry (I_h), the design of organic ligands that induce chirality into the Au_{13} cluster is the only viable option. Inspired by pioneering studies, chiral organic ligands have been employed to induce chirality in gold nanoclusters [19–21]. Herein, we report the total structure of a Au_{13} cluster covered by five 1,2-bis(diphenylphosphino)ethane (dppe) and two chlorine ligands, $[Au_{13}(dppe)_5Cl_2]^{3+}$ (hereafter denoted as Au_{13}). The architecture of the dppe binding pattern made the whole cluster chiral with a propeller-like arrangement. Analyses showed that the Au_{13} clusters demonstrate strong near-infrared photoluminescence properties and the ability to sensitize singlet oxygen ($^1O_2$) photogeneration with markedly higher quantum yields than other gold nanoclusters.

2 Experimental

2.1 Chemicals

All chemicals, including solvents, were commercially available as reagent grade and used as received without further purification. $Au_2(dppe)Cl_2$ (98%), Na_2S (97%), and $NaBH_4$ (99%) were purchased from Adamas. Ultrapure

water (resistance, 18.2 MΩ·cm) was purified with a Barnstead Nanopure Di-water TM system. All glassware was thoroughly cleaned with aqua regia (37 wt.% HCl:HNO_3 = 3:1, v/v), rinsed copiously with nanopure water, and then dried in an oven prior to use.

2.2 Synthesis of $[Au_{13}(dppe)_5Cl_2]Cl_3$ cluster

All manipulations were performed in air. Na_2S (2 mg) dissolved in MeOH (2 mL) was added to $Au_2(dppe)Cl_2$ (126.1 mg, 0.1 mmol) in CH_2Cl_2 (20 mL) and then stirred vigorously for 1 h, during which the solution changed from colorless to yellow. Next, a freshly prepared solution of $NaBH_4$ (3.8 mg, 0.1 mmol) in ice water (1 mL) was added and the solution rapidly turned dark red. The reaction mixture was then stirred for 2.5 h. Solvent was removed under reduced pressure to give a black solid. The black solid was washed with hexane/CH_2Cl_2 (5:1, v/v). The solid was then dissolved in EtOH (20 mL) and stirred for 24 h at 30 °C. Solvent was removed under reduced pressure to give a black solid. The black solid was washed sequentially with H_2O, hexane/CH_2Cl_2 (5:1, v/v), and acetone to obtain the Au_{13} clusters. The clusters (10 mg) were redissolved in ethanol (3 mL) and single crystals suitable for synchrotron radiation X-ray diffraction were grown by slow evaporation. After crystallization, Au_{13} clusters were obtained as black crystals.

2.3 Synchrotron radiation X-ray crystallographic structural determinations

Suitable single crystals were selected and synchrotron radiation X-ray diffraction data was collected at the BL14B1 beamline of the Shanghai Synchrotron Radiation Facility (SSRF), China, using a constant wavelength of λ = 0.65248 Å and a large Debye– Scherrer camera. Data reduction, cell refinement, and experimental absorption correction were performed using HKL-3000 and Agilent Gemini Ultra CrysAlisPro software packages (Ver. 1.171.35.11). Structures were solved by intrinsic phasing and refined against F^2 by full-matrix least-squares. All non-hydrogen atoms were refined anisotropically. Hydrogen atoms were generated geometrically. All calculations were carried out using SHELXT [22] and Olex2 ver. 1.2.8 [23] software packages.

CCDC-1548942 contains supplementary crystallographic data for $[Au_{13}(dppe)_5Cl_2]Cl_3$ reported in this paper. These data can be obtained free of charge from Cambridge Crystallographic Data Centre via https://www.ccdc.cam.ac.uk/structures/.

2.4 Characterization

UV/Vis spectra were measured in methanol using an Agilent Cary 300 spectrophotometer. Mass spectra were obtained using an ion trap mass spectrometer (Thermofisher LTQ) in positive mode (capillary voltage, 33 V). The sample solution (in acetonitrile) was infused into the electrospray ionization (ESI) source at a flow rate of 300 $\mu L \cdot min^{-1}$. X-ray photoelectron spectroscopy (XPS) measurements were performed under ultrahigh vacuum (UHV, 1.0 × 10^{-7} Torr), an axis HS monochromatized Al Kα cathode source of 150 W, a focused X-ray 100-μm beam, a pass energy of 55 eV with 0.1-eV step length, and a detect angle (take off) of 45° on an X-ray microprobe (ULVAC-PHI Quantera SXM). The binding energy was calibrated with that of C1s (284.8 eV). Ultraviolet photoemission spectroscopy (UPS) was performed on Omicron HA100 electron energy analyzer using a UVS 300 high-current UV lamp with an excitation energy of He II (40.8 eV). The solid sample was loaded onto indium-tin oxide (ITO) glass before testing.

2.5 Spectroscopic detection of $^1O_2$

Au clusters were dissolved in dichloromethane (~ 2 mL), bubbled with either ultra-high purity N_2 or O_2 gas, and sealed in a gas-tight cuvette with a Teflon stopper. Photoluminescence (PL) spectra were recorded on a Horiba Fluorolog 3 spectrofluorometer at 800–1,500 nm using a liquid-N_2-cooled InGaAs detector, an excitation wavelength of 350 nm, 14.7-nm slits, and a 550-nm long-pass optical filter between the sample and the detector to block overtones from the excitation source.

2.6 Measurement of $^1O_2$ quantum yield

For $^1O_2$ assessment using 1,3-diphenyl isobenzofuran (DPBF) as the probe, a stock solution of 1 mM DPBF in $CHCl_3$ was prepared. The stock solution was added to a solution of Au_{13} or anthracene in $CHCl_3$ (1 mL) to give final concentrations of 3 μM for Au_{13} and anthracene and 70 μM for DPBF. The solutions were purged with air for 5 min immediately prior to measurement and then irradiated with a 365-nm light-emitting device (LED). Adsorption spectra were recorded after different periods of light irradiation.

2.7 Computational details

Density functional theory (DFT) calculations were carried out using the Gaussian09 program package and B3PW91 hybrid density functional. LANL2DZ (Au atoms) and 6-31G** (C, H, P, and Cl atoms) basis sets were employed [24–27]. Time-dependent DFT (TD-DFT) calculations were performed to obtain stimulated UV/Vis and CD spectra.

3 Results and discussion

3.1 Synthesis and crystal structure of $[Au_{13}(dppe)_5Cl_2]^{3+}$ nanocluster

The Au_{13} cluster was synthesized by reducing the diphosphine-protected $Au^I_2(dppe)Cl_2$ motif as a precursor using a double-reducing agent, such as Na_2S and $NaBH_4$, under vigorous stirring. Notably, in this kind of size-focusing methodology, only the most robust species survived, while other species were either decomposed or converted to the most stable species. In this synthetic methodology, the most stable structure from a geometric perspective, Au_{13} with icosahedral topology, was the only and most likely nanocluster species to survive. Solvent removal produced black solids that were recrystallized in ethanol to yield small (approx. 0.05 mm) black block-shaped crystals. The size of the cluster crystals was below the limit of laboratory-based single-crystal X-ray diffraction methods; therefore, synchrotron radiation X-ray diffraction was used to resolve the nanocluster structural framework [28].

The structure of the gold cluster was found to contain an Au_{13} core wrapped with five equatorial dppe ligands and two axial Cl atoms (Fig. 1). The topological structure of the Au_{13} kernel was first reported by Mingos [29] in 1981 for an $[Au_{13}(PMe_2Ph)_{10}Cl_2](PF_6)_3$ cluster employing a monodentate phosphine as the protecting ligand. Furthermore, Konishi reported similar nanoclusters capped with bidentate phosphine ligands, $[Au_{13}(dppe)_5Cl_2]Cl_3$ [30–31] and $[Au_{13}(dppe)_5(C{\equiv}CPh)_2]^{3+}$ [32]. However, these previous reports of similar Au_{13} kernel structures showed that the minimum asymmetric units all possessed high symmetry, with only half or one $Au_{13}(dppe)_5Cl_2$ unit discovered [29–32]. Therefore，it was not possible to observe chiral enantiomers of the Au_{13} clusters. In our study, five $Au_{13}(dppe)_5Cl_2$ nanoclusters were found in the crystal unit cell, making the *c*-axis direction of the crystal as long as 70.68 Å by synchrotron radiation X-ray diffraction analysis. The $Au_{13}(dppe)_5Cl_2$ cluster can be considered as two pentagonal Au_6 bipyramids linked together via the central gold atom (Au_1, Fig. 2(a)). The two Au_6 bipyramids possessed ideal D_{5h} symmetry and were twisted relative to each other by about 36□. Gold atoms at the tip of the bipyramids were ligated by Cl atoms. The other ten surface gold atoms of the bipyramids were covered with five dppe ligands, with each dppe ligand coordinated with two gold atoms from both bipyramids.

The bond lengths (e.g., Au–Au, Au–S, and S–C) and angles of the $[Au_{13}(dppe)_5Cl_2]^{3+}$ cluster are shown in Table 1 and compared with those of $[Au_{13}(PPhMe_2)_{10}Cl_2]^{3+}$ (Fig. S1 in the Electronic Supplementary Material (ESM)). Notably, the $[Au_{13}(PMe_2Ph)_{10}Cl_2](PF_6)_3$ cluster was achiral. The average $Au_{(staple)}$–$Au_{(central)}$ bond length in $[Au_{13}(dppe)_5Cl_2]^{3+}$ was shorter than that in $[Au_{13}(PPhMe_2)_{10}Cl_2]^{3+}$ (2.552 and 2.679 Å, respectively; Table 1, entry 1). This indicated that the Au_{13} core size in $[Au_{13}(dppe)_5Cl_2]^{3+}$ was smaller (4.7%) than that in $[Au_{13}(PPhMe_2)_{10}Cl_2]^{3+}$. Furthermore, the $Au_{(Cl)}$–$Au_{(center)}$–$Au_{(Cl)}$, Cl–$Au_{(center)}$–Cl, and $Au_{(P)}$ –$Au_{(center)}$–$Au_{(opposite)}$ angles in the $[Au_{13}(dppe)_5Cl_2]^{3+}$ clusters were 178.81□, 177.99□, and 178.92□, respectively (Table 1, entries 2–4). The Cl–Au–Au–Cl torsion angle was 177.51□. These results suggested that the icosahedral Au_{13} core of $[Au_{13}(dppe)_5Cl_2]^{3+}$ was distorted, forming the chiral arrangement.

Table 1 Comparison of average bond lengths and angles in clusters of $[Au_{13}(PPhMe_2)_{10}Cl_2]^{3+}$ [26] and $[Au_{13}(dppe)_5Cl_2]^{3+}$ (this work)

Entry	Average lengths and angles	$[Au_{13}(dppe)_5Cl_2]^{3+}$	$[Au_{13}(PPhMe_2)_{10}Cl_2]^{3+}$
1	$Au_{(staple)}$–$Au_{(center)}$	2.552 Å (2.486–2.597 Å)	2.679 Å (2.715–2.788 Å)
2	Angle of $Au_{(Cl)}$–$Au_{(center)}$–$Au_{(Cl)}$	178.81°	180°
3	Angle of Cl–$Au_{(center)}$–Cl	177.99°	180°
4	Angle of $Au_{(P)}$–$Au_{(center)}$–$Au_{(opposite)}$	178.92° (177.99°–179.27°)	180°
5	Torsion angle of Cl–Au–Au–Cl	177.51°	180°

From further careful structural examination of $[Au_{13}(dppe)_5Cl_2]$, its intrinsic chirality was interpreted using symmetry reduction, which demonstrated that the ideal icosahedral Au_{13} kernel possessed I_h point group symmetry. This symmetry would be reduced to the highest possible C_{3v} symmetry when two Cl atoms are anchored in polar axial positions. The highest possible symmetry will be further reduced to the C_s point group if the ten equatorial and axial positions are ligated by P atoms, which are free without restriction. However, such satiation cannot occur for diphosphine ligands with the P pair bridged by alkyl chains (–$CH_2CH_2CH_2$–), which obviously twist to generate a chiral ansa metallamacrocycle and finally reduce to give C_1 symmetry (Fig. 3).

The relative twist of the two bipyramids induced a helical arrangement in the five pairs of P atoms on the Au_{13} cluster surface. The helical arrangement could be in a clockwise (C) or anticlockwise (A) manner, which corresponded to the two different enantiomers found in the nanocluster crystal structure (Fig. S2 in the ESM). Taking one of the five monomers from the single crystal unit cell, the chiral ansa metallamacrocycle, Au–P–C–C–P–Au, was represented as polyhedral, with each petal of five metallamacrocycles in $[Au_{13}(dppe)_5Cl_2]^{3+}$ arranged in an anticlockwise propeller pattern from the top view (Fig. 2(b)). However, the enantiomers of the Au_{13} nanoclusters were co-crystallized to give a racemic mixture with a non-centrosymmetric space group of *Cc* containing five monomers (Flack parameter = 0.302) [33]. Our analysis showed that the racemic mixture of

the Au_{13} nanoclusters was silent in circular dichroism (CD) spectroscopy, as expected. Two types of π–π stacking interactions were observed among phenyl rings in the $[Au_{13}(dppe)_5Cl_2]^{3+}$ nanocluster: (1) a sandwich configuration, which maximizes overlap of the π systems of phenyl rings in two neighboring dppe ligands (*d* = 2.83–2.89 Å, Fig. S3(a) in the ESM); and (2) an edge-to-face configuration, which contains neighboring phenyl rings that are perpendicular to each other (*d* = 4.15–4.2 Å, Fig. S3(b) in the ESM). Furthermore, the Au_{13} clusters were packed with each other via intercluster ligand interactions, including CH···π and π···π stacking (Fig. S4 in the ESM). The CH···π interactions ranged from 2.200 to 2.440 Å, while π···π interactions ranged from 2.997 to 3.238 Å.

3.2 Characterization of $[Au_{13}(dppe)_5Cl_2]Cl_3$ nanocluster

The as-obtained nanoclusters were fully characterized by UV/Vis, ESI-TOF-MS, XPS, and UPS analyses. Only one ion peak at *m*/*z* = 1,541.1 with *z* = 3 was observed by ESI-TOF-MS analysis, which well matched the molecular weight of the $[Au_{13}(dppe)_5Cl_2]^{3+}$ cluster ($Au_{13}P_{10}C_{130}H_{120}Cl_2$, theoretical *m*/*z* = 1,541.2) and agreed with simulated patterns (Fig. 4).

The UV/Vis absorption spectrum of $[Au_{13}(dppe)_5Cl_2]^{3+}$ dissolved in CH_2Cl_2 contained two prominent absorption bands at 383 and 488 nm (Fig. 5), which were consistent with previous reports [29–32]. XPS analysis confirmed the presence of only Au, P, and Cl atoms in the Au_{13} sample (Fig. S5 in the ESM), in addition to residual oxygen atoms from exposure to ambient conditions. The P 2p binging energy appeared at 132.96 eV (Fig. 6(a)). The nanocluster Au 4f7/2 binding energy (84.38 eV, Fig. 6(b)) was upshifted from Au foil by approximately 0.4 eV, but was 0.5 eV lower than that of the Au(PPh3)2Cl complex [34]. These results indicated that the Au species were positively charged ($Au^{\delta+}$, where $0 < \delta < 1$).

DFT calculations provided further insight into the electronic and optical properties of Au_{13} nanoclusters. The theoretical optical absorption spectrum of $[Au_{13}(PH_2CH_2CH_2PH_2)_5Cl_2]^{3+}$ was modeled by replacing the phenyl

rings with hydrogen atoms. The calculated highest occupied molecular orbital (HOMO)–lowest unoccupied molecular orbital (LUMO) gap of $[Au_{13}(dppe)_5Cl_2]^{3+}$ was found to be 1.9 eV, which agreed with the experimental result (1.9 eV). The calculated UV/Vis spectrum of the model was in good agreement with the experimental results, especially the spectral shape (Fig. 5).

Intrinsic chirality analysis of the $[Au_{13}(dppe)_5Cl_2]^{3+}$ cluster was performed by symmetry reduction and structural perspective. To explore its chirality, we attempted attempted to obtain enantiopure product from the mixed $[Au_{13}(dppe)_5Cl_2]^{3+}$ enantiomers using chiral high-performance liquid chromatography (HPLC) [35, 36]. Unfortunately, such resolution was not successful for the C2 birdied $[Au_{13}(dppe)_5Cl_2]^{3+}$ cluster, which might be due to the low energy barrier of the small six-membered-ring-based chiral ansa metallamacrocycle, Au–P–C2–P–Au. Therefore, fast racemization may occur, leading to HPLC chiral resolution failing [37, 38]. Therefore, larger chiral ansa metallamacrocycles employing similar structural ligands, 1,6-bis(diphenylphosphino)hexane (C6, dpph) and 1,5-bis(diphenylphosphino)pentane (C5, dppp), were designed to form Au–P-–C6–P–Au ten-membered and Au–P–C5–P–Au nine-membered rings. These structures might increase the energy barrier to avoid fast racemization, leading to successful chiral resolution. However, Au_{13} clusters were not achieved under an identical synthetic protocol using dpph and dppp as the protecting ligand. Therefore, as a compromise, to obtain indirect evidence of chirality, simulated electronic circular dichroism (ECD) was conducted by TD-DFT calculations to investigate the intrinsic nature of the $[Au_{13}(dppe)_5Cl_2]^{3+}$ cluster.

The CD spectra of the two enantiomers were approximate mirror images of each other. These results also indicated that racemization occurred during crystallization, which made the as-synthesized Au_{13} nanoclusters silent under experimental CD spectroscopy. The simulated ECD of Au_{13} clusters matched well with the corresponding absorption bands in the UV/Vis spectrum, namely, the theoretical band at around 385 nm, while the band around 490 nm split into two bands located at 470 and 560 nm due to the Cotton effect (Fig. 7(a)). A similar phenomenon has been observed in chiral Au complexes and clusters, such as Au_6, Au_8, and Au_{11} [39, 40], and polyoxometalate organic hybrids [37]. The concentration-independent anisotropy factor (*g* factor) was up to

10^{-3}, which was comparable to typical chiral organic molecules and other ligand-protected gold nanoclusters [35, 36]. The maximum and characteristic anisotropy factor of the $[Au_{13}(dppe)_5Cl_2]^{3+}$ cluster was 4.69 x 10^{-3} at around 385 nm, while the anisotropy factors were about 1.22 x 10^{-3} and 1.81 x 10^{-3} at 470 and 560 nm, respectively. (Fig. 7(b))

Next, UPS analysis was used to investigate the surface electronic structure of the $[Au_{13}(dppe)_5Cl_2]^{3+}$ cluster, such as the chemical nature of ligands. In particular, the characteristics of the density of states of the 6s and 5d bands can be seen in the valence band spectrum of the gold clusters [41–43]. In previous reports, the intensity of the $5d_{5/2}$ orbital features in a thiolate-protected $Au_{38}(SR)_{24}$ cluster appeared at about 3.4 eV in UPS analysis [43].

As shown in Fig. 8(a), valence band photoemission of the Au_{13} nanoclusters showed a higher binding energy for the gold d-band at 3.9 eV due to the presence of partially oxidized Au atoms, as supported by XPS analysis. The valence band region (from 0 to approx. 5 eV), also called the HOMO–LUMO gap region, was further determined to be approx. 1.9 eV (Fig. 8(b)). This was highly consistent with the optical energy gap calculated from the UV/Vis spectrum and DFT calculations (1.9 eV).

3.3 $^1O_2$ generation by photoexcitation of $[Au_{13}(dppe)_5Cl_2]^{3+}$ nanoclusters

Recently, gold nanoclusters have been well explored in a variety of applications, e.g., photosensitizer for $^1O_2$ generation [44–49]. Singlet oxygen is a chemically reactive molecule and widely applied in photodynamic therapy (PDT) for cancer treatment, water purification, oxidation catalysis, and other fields [50]. The Au_{13} cluster HOMO–LUMO gap of approx. 1.9 eV was larger than the activation energy of molecular oxygen ($^3O_2 \rightarrow {}^1O_2$, ΔE = +0.97 eV), opening up a potential application in $^1O_2$ photogeneration. To test this hypothesis, near-infrared (NIR) PL spectroscopy was employed for direct detection of $^1O_2$ generation using the Au_{13} clusters as photosensitizers.

Figure 9 shows NIR PL spectra of a CH_2Cl_2 solutions of Au_{13} that are either N_2-purged (black curve) or

O_2-saturated (red curve). The Au_{13} PL spectrum contained a main emission peak centered at approx. 982 nm (~ 1.26 eV, Fig. 9(a)). The introduction of O_2 decreased the Au_{13} PL intensity between 1,260 and 1,290 nm and produced a small PL peak at 1,276 nm (0.97 eV, Fig. 9(a), inset). This represented the radiative relaxation of $^1O_2$ back to ground state $^3O_2$. Both these spectral changes provided evidence that Au_{13} nanoclusters can generate $^1O_2$ upon photoexcitation. The peak disappeared and was reproduced upon cycling between N_2 and O_2 gas (Fig. S6 in the ESM). Notably, Konishi reported an identical Au_{13} gold nanocluster that emitted at 766 nm in acetonitrile, while no NIR emission was observed. Meanwhile, the Au_{13} gold nanocluster in CH_2Cl_2 possessed an obvious NIR PL property (982 nm, Fig. 9(a)). This difference might be attributed to the different packing styles in difference solvents, which has been found in a similar nanocluster system [51]. Furthermore, a $^1O_2$ quantum yield of $\Phi_{Au13} = 0.71$ was estimated for the Au_{13} clusters relative to an anthracene standard using DPBF as probe (Scheme S1 and Fig. S7 in the ESM). This Φ_{Au13} was considerably higher than those reported for $Au_{25}(SR)_{18}$ ($\Phi_{Au25} = 0.17$) and $Au_{38}S_2(SAdm)_{20}$ ($\Phi_{Au38} = 0.22$) gold nanoclusters (Fig. S8 in the ESM) [44, 45], which might be due to the relatively large HOMO− LUMO gap (1.9 eV) of the Au_{13} nanocluster (Au_{25} cluster, 1.3 eV; Au_{38}, 1.57 eV).

We have proposed a tentative mechanism of singlet oxygen generation via gold nanocluster photoexcitation, which involves a Dexter-type electron exchange coupling between the excited photosensitizer and ground-state triplet oxygen molecules [52]. $[Au_{13}(dppe)_5Cl_2]^{3+}$ nanoclusters at their ground state (S_0) may become excited to a different singlet state with a greater energy content (S_1) by absorbing light. Some of the excited Au_{13} nanoclusters may undergo intersystem crossing (ISC) to convert to a slightly lower energy level (T_1) via spin flipping of the excited electron. $^3O_2$ can exchange an electron, resulting in the formation of $^1O_2$ and returning the Au_{13} nanoclusters back to the ground state. In other words, the photon energy is transferred to electrons in the photosensitizer Au_{13} nanoclusters, these light-excited photoelectrons can then travel to the triplet state and eventually contribute to $^1O_2$ production via energy transfer from Au_{13}

nanoclusters to $^3O_2$, leading to conversion of chemical probe DPBF into 1,4- diphenyl-1,4,4a,8a- tetrahydro-1,4-epoxybenzo[d][1,2]dioxine (Fig. 10).

To gain further insight, we compared the photocatalytic activity of the $[Au_{13}(dppe)_5Cl_2]^{3+}$ and $[Au_{11}(PPh_3)_7Cl_3]^+$ nanoclusters. The latter nanocluster exhibited an incomplete centered icosahedral skeleton with HOMO–LUMO gap of approx. 2.0 eV (Figs. S9– S11 in the ESM) [15, 16, 50]. The Au_{11} nanoclusters showed a broad NIR PL peak at around 1,080 nm (approx. 1.15 eV, Fig. 9(b)). O_2-saturated solutions of Au_{11} nanoclusters do not show characteristic $^1O_2$ PL (1,270–1,280 nm, Fig. 9(b), inset), indicating that the Au_{11} cluster was not photocatalytically active. Notably, the Au_{11} nanocluster were stable in CH_2Cl_2 solution under 365-nm irradiation for 2 h (Fig. S12 in the ESM).

These results demonstrated that the photoexcited Au_{13} cluster can produce singlet oxygen, while the Au_{11} cluster cannot afford singlet oxygen. Both Au_{13} and Au_{11} clusters have eight-electron structures, and the Au_{11} cluster had a suitable optical energy gap of 2.1 eV. Au_{11} does not sensitize $^3O_2$ to afford $^1O_2$ may be due to its low quantum yield. Notably, the quantum yield of Au_{11} has yet to be reported. However, the quantum yield of structural analogue alloy nanocluster $PdAu_{10}(PPh_3)_8Cl_2$ was approx. 1.59×10^{-3} [53], which was much lower than that of the Au_{13} cluster with a high quantum yield of $\Phi_{Au13} = 0.71$.

4. Conclusions

In summary, diphosphine-ligand-capped Au_{13} nanoclusters, $[Au_{13}(dppe)_5Cl_2]^{3+}$, were synthesized. The crystal structure of the cluster was determined using a synchrotron radiation X-ray diffraction method (single crystal size, approx. 0.05 mm), which showed a propeller arrangement framework. The molecular structure of the nanocluster was further characterized using UV/Vis spectroscopy, ESI-MS, XPS, UPS, and DFT calculations, and the HOMO–LUMO gap of the cluster was determined to be approx. 1.9 eV. The bidentate feature of the diphosphine ligands led to a helical arrangement of capping ligands, which made the Au_{13} clusters a chiral species. Finally, the near- infrared photoluminescence properties of the Au_{13} clusters were investigated, with the

results showing that the Au_{13} nanoclusters can be employed as efficient photosensitizers for singlet oxygen generation with a high quantum yield of $\Phi_{Au13} = 0.71$.

Acknowledgements

G. L. acknowledges financial supports by the fund of the National Natural Science Foundation of China (No. 21701168) and the Liaoning Natural Science Foundation (No. 20170540897), and beamline BL14B (Shanghai Synchrotron Radiation Facility) for providing the beam time. A portion of this report was prepared as an account of work sponsored by an agency of the United States Government (D. R. K.). Neither the United States Government nor any agency thereof, nor any of their employees, makes any warranty, express or implied, or assumes any legal liability or responsibility for the accuracy, completeness, or usefulness of any information, apparatus, product, or process disclosed, or represents that its use would not infringe privately owned rights.

Electronic Supplementary Material: Supplementary material (including the structural elucidation, XPS spectra, photoluminescence spectra, $^1O_2$ quantum yield measurement, and UV/Vis spectra) is available in the online version of this article at https://doi.org/10.1007/ s12274-017-1935-2.

References

[1] Jin, R. C.; Zeng, C. J.; Zhou, M.; Chen, Y. X. Atomically precise colloidal metal nanoclusters and nanoparticles: Fundamentals and opportunities. *Chem. Rev.* **2016**, *116*, 10346−10413.

[2] Yamazoe, S.; Koyasu, K.; Tsukuda, T. Nonscalable oxidation catalysis of gold clusters. *Acc. Chem. Res*. **2014**, *47*, 816−824.

[3] Fang, J.; Zhang, B.; Yao, Q. F.; Yang, Y.; Xie, J. P.; Yan, N. Recent advances in the synthesis and catalytic applications of ligand-protected, atomically precise metal nanoclusters. *Coord. Chem. Rev.* **2016**, *322*, 1–29.

[4] Li, G.; Jin, R. C. Atomically precise gold nanoclusters as new model catalysts. *Acc. Chem. Res*. **2013**, *46*, 1749−1758.

[5] Pensa, E.; Cortés, E.; Corthey, G.; Carro, P.; Vericat, C.; Fonticelli, M. H.; Benitez, G.; Rubert, A. A.; Salvarezza, R. C. The chemistry of the sulfur–gold interface: In search of a unified model. *Acc. Chem. Res*. **2012**, *45*, 1183−1192.

[6] Yu, Y.; Luo, Z. T.; Chevrier, D. M.; Leong, D. T.; Zhang, P.; Jiang, D. E.; Xie, J. P. Identification of a highly luminescent $Au_{22}(SG)_{18}$ nanocluster. *J. Am. Chem. Soc.* **2014**, *136*, 1246–1249.

[7] Liu, P. X.; Qin, R. X.; Fu, G.; Zheng, N. F. Surface coordination chemistry of metal nanomaterials. *J. Am. Chem. Soc.* **2017**, *139*, 2122−2131.

[8] Li, G.; Abroshan, H.; Liu, C.; Zhuo, S.; Li, Z. M.; Xie, Y.; Kim, H. J.; Rosi, N. L.; Jin, R. C. Tailoring the electronic and catalytic properties of Au_{25} nanoclusters via ligand engineering. *ACS Nano* **2016**, *10*, 7998–8005.

[9] Mingos, D. M. P. *Gold Clusters, Colloids and Nanoparticles I*; Springer: Switzerland, 2014.

[10] Zeng, C. J.; Chen, Y. X.; Kirschbaum, K.; Lambright, K. J.; Jin, R. C. Emergence of hierarchical structural complexities in nanoparticles and their assembly. *Science* **2016**, *354*, 1580–1584.

[11] Qian, H. F.; Eckenhoff, W. T.; Zhu, Y.; Pintauer, T.; Jin, R. C. Total structure determination of thiolate-protected Au_{38} nanoparticles. *J. Am. Chem. Soc.* **2010**, *132*, 8280–8281.

[12] Crasto, D.; Malola, S.; Brosofsky, G.; Dass, A.; Häkkinen, H. Single crystal XRD structure and theoretical analysis of the chiral $Au_{30}S(S\text{-}t\text{-}Bu)_{18}$ cluster. *J. Am. Chem. Soc.* **2014**, *136*, 5000–5005.

[13] Chen, J.; Zhang, Q. F.; Bonaccorso, T. A.; Williard, P. G.; Wang, L. S. Controlling gold nanoclusters by diphospine ligands. *J. Am. Chem. Soc.* **2014**, *136*, 92–95.

[14] Lopez-Acevedo, O.; Tsunoyama, H.; Tsukuda, T.; Häkkinen, H.; Aikens, C. M. Chirality and electronic structure of the thiolate-protected Au_{38} nanocluster. *J. Am. Chem. Soc.* **2010**, *132*, 8210−8218.

[15] McKenzie, L. C.; Zaikova, T. O.; Hutchison, J. E. Structurally similar triphenylphosphine-stabilized undecagolds, $Au_{11}(PPh_3)_7Cl_3$ and $[Au_{11}(PPh_3)_8Cl_2]Cl$, exhibit distinct ligand exchange pathways with glutathione. *J. Am. Chem. Soc.* **2014**, *136*, 13426−13435.

[16] Gutrath, B. S.; Englert, U.; Wang, Y. T.; Simon, U. A missing link in undecagold cluster chemistry: Single-crystal X-ray analysis of $[Au_{11}(PPh_3)_7Cl_3]$. *Eur. J. Inorg. Chem.* **2013**, *2013*, 2002−2006.

[17] Yan, J. Z.; Su, H. F.; Yang, H. Y.; Hu, C. Y.; Malola, S.; Lin, S. C.; Teo, B. K.; Häkkinen, H.; Zheng, N. F. Asymmetric synthesis of chiral bimetallic $[Ag_{28}Cu_{12}(SR)_{24}]^{4-}$ nanoclusters via ion pairing. *J. Am. Chem. Soc.* **2016**, *138*, 12751–12754.

[18] Wan, X. K.; Yuan, S. F.; Lin, Z. W.; Wang, Q. M. A chiral gold nanocluster Au_{20} protected by tetradentate phosphine ligands. *Angew. Chem., Int. Ed.* **2014**, *53*, 2923–2926.

[19] Qian, H. F.; Zhu, M. Z.; Gayathri, C.; Gil, R. R.; Jin, R. C. Chirality in gold nanoclusters probed by NMR spectroscopy. *ACS Nano* **2011**, *5*, 8935–8942.

[20] Zhu, M. Z.; Qian, H. F.; Meng, X. M.; Jin, S. S.; Wu, Z. K.; Jin, R. C. Chiral Au_{25} nanospheres and nanorods: Synthesis and insight into the origin of chirality. *Nano Lett.* **2011**, *11*, 3963–3969.

[21] Xu, Q.; Kumar, S.; Jin, S. S.; Qian, H. F.; Zhu, M. Z.; Jin, R. C. Chiral 38-gold-atom nanoclusters: Synthesis and chiroptical properties. *Small* **2014**, *10*, 1008–1014.

[22] Sheldrick, G. M. *SHELXT*-integrated space-group and crystal-structure determination. *Acta Cryst.* **2015**, *A71*, 3−8.

[23] Dolomanov, O. V.; Bourhis, L. J.; Gildea, R. J.; Howard, J. A. K.; Puschmann, H. *OLEX2*: A complete structure solution, refinement and analysis program. *J. Appl. Cryst.* **2009**, *42*, 339–341.

[24] Becke, A. D. Density-functional exchange-energy approximation with correct asymptotic-behavior. *Phys. Rev. A* **1988**, *38*, 3098–3100.

[25] Becke, A. D. Density-functional thermochemistry. III. The role of exact exchange. *J. Chem. Phys.* **1993**, *98*, 5648–5652.

[26] Burant, J. C.; Scuseria, G. E.; Frisch, M. J. A linear scaling method for hartree-fock exchange calculations of large molecules. *J. Chem. Phys*. **1996**, *105*, 8969–8972.

[27] Frisch, M. J.; Trucks, G. W.; Schlegel, H. B.; Scuseria, G. E.; Robb, M. A.; Cheeseman, J. R.; Scalmani, G.; Barone, V.; Mennucci, B.; Petersson, G. A. et al. *Gaussian 09*, Revision A.1; Gaussian, Inc.: Wallingford, CT, USA, 2009.

[28] $C_{650}H_{600}P_{50}Cl_{10}Au_{65}$, M_r = 23,117.76, monoclinic, space group *C/c*, *a* = 29.113(6) Å, *b* = 29.569(6) Å, *c* = 70.683(14) Å, β = 101.61(3)°, V = 59602(21) Å^3, Z = 4, T = 293(2) K, 81,277 reflections measured, R_1(final) = 0.0830, wR_2 = 0.1931. CCDC-1548942, contain the supplementary crystallographic data for this paper. These data can be obtained free of charge from The Cambridge Crystallographic Data Centre via www.ccdc.cam.ac.uk/data_request/cif.

[29] Briant, C. E.; Theobald, B. R. C.; White, J. W.; Bell, L. K.; Mingos, D. M. P.; Welch, A. J. Synthesis and X-ray structural characterization of the centred icosahedral gold cluster compound $[Au_{13}(PMe_2Ph)_{10}Cl_2](PF_6)_3$: The realization of a theoretical prediction. *J. Chem. Soc., Chem. Commun*. **1981**, 201−202.

[30] Shichibu, Y.; Konishi, K. HCl-induced nuclearity convergence in diphosphine-protected ultrasmall gold clusters: A novel synthetic route to "magic-number" Au_{13} clusters. *Small* **2010**, *6*, 1216–1220.

[31] Shichibu, Y.; Suzuki, K.; Konishi, K. Facile synthesis and optical properties of magic-number Au_{13} clusters. *Nanoscale* **2012**, *4*, 4125−4129.

[32] Sugiuchi, M.; Shichibu, Y.; Nakanishi, T.; Hasegawa, Y.; Konishi, K. Cluster–π electronic interaction in a superatomic Au_{13} cluster bearing σ-bonded acetylide ligands. *Chem. Commun*. **2015**, *51*, 13519−13522.

[33] Flack, H. D.; Bernardinelli, G. Absolute structure and absolute configuration. *Acta Cryst.* **1999**, *A55*, 908–915.

[34] Yamamoto, Y.; Konno, H. Ylide-metal complexes. X. An X-ray photoelectron spectroscopic study of triphenylmethylenephosphorane and gold- and copper-phosphorane complexes. *Bull. Chem. Soc. Jpn*. **1986**, *59*, 1327−1330.

[35] Dolamic, I.; Knoppe, S.; Dass, A.; Bürgi, T. First enantioseparation and circular dichroism spectra of Au_{38} clusters protected by achiral ligands. *Nat. Commun.* **2012**, *3*, *798*.

[36] Dolamic, I.; Varnholt, B.; Bürgi, T. Chirality transfer from gold nanocluster to adsorbate evidenced by vibrational circular dichroism. *Nat. Commun.* **2015**, *6*, *7117*.

[37] Zhang, J. W.; Luo, J. H.; Wang, P. M.; Ding, B.; Huang, Y. C.; Zhao, Z. L.; Zhang, J.; Wei, Y. G. Step-by-step strategy from achiral precursors to polyoxometalates-based chiral organic-inorganic hybrids. *Inorg. Chem.* **2015**, *54*, 2551–2559.

[38] Zhang, J. W.; Huang, Y. C.; Zhang, J.; She, S.; Hao, J.; Wei, Y. G. A direct anchoring of Anderson-type polyoxometalates in aqueous media with tripodal ligands especially containing the carboxyl group. *Dalton Trans.* **2014**, *43*, 2722–2725.

[39] He, X.; Wang, Y. C.; Jiang, H.; Zhao, L. Structurally well-defined sigmoidal gold clusters: Probing the correlation between metal atom arrangement and chiroptical response. *J. Am. Chem. Soc.* **2016**, *138*, 5634−5643.

[40] Takano, S.; Tsukuda, T. Amplification of the optical activity of gold clusters by the proximity of BINAP. *J. Phys. Chem. Lett*. **2016**, *7*, 4509−4513.

[41] Ji, M.; Gu, X.; Li, X.; Gong, X. G.; Li, J.; Wang, L. S. Experimental and theoretical investigation of the electronic and geometrical structures of the Au_{32} cluster. *Angew. Chem., Int. Ed.* **2005**, *44*, 7119–7123.

[42] Liu, J.; Krishna, K. S.; Losovyj, Y. B.; Chattopadhyay, S.; Lozova, N.; Miller, J. T.; Spivey, J. J.; Kumar, C. S. S. R. Ligand-stabilized and atomically precise gold nanocluster catalysis: A case study for correlating fundamental electronic properties with catalysis. *Chem.—Eur. J.* **2013**, *19*, 10201– 10208.

[43] Losovyj, Y. B.; Li, S.-C.; Lozova, N.; Katsiev, K.; Stellwagen, D.; Diebold, U.; Kong, L.; Kumar, C. S. S. R. Evidence for s–d hybridization in Au_{38} clusters. *J. Phys. Chem. C* **2012**, *116*, 5857–5861.

[44] Kawasaki, H.; Kumar, S.; Li, G.; Zeng, C. J.; Kauffman, D. R.; Yoshimoto, J.; Iwasaki, Y.; Jin, R. C. Generation of singlet oxygen by photoexcited $Au_{25}(SR)_{18}$ clusters. *Chem. Mater.* **2014**, *26*, 2777−2788.

[45] Li, Z. M.; Liu, C.; Abroshan, H.; Kauffman, D. R.; Li, G. $Au_{38}S_2(SAdm)_{20}$ photocatalyst for one-step selective aerobic oxidations. *ACS Catal*. **2017**, *7*, 3368–3374

[46] Zhou, Y.; Li, G. A critical review on carbon-carbon coupling over ultra-small gold nanoclusters. *Acta Phys.-Chim. Sin*. **2017**, *33*, 1297−1309.

[47] Chen, H. J.; Liu, C.; Wang, M.; Zhang, C. F.; Luo, N. C.; Wang, Y. H.; Abroshan, H.; Li, G.; Wang, F. Visible light gold nanocluster photocatalyst: Selective aerobic oxidation of amines to imines. *ACS Catal*. **2017**, *7*, 3632–3638.

[48] Zhang, C. L.; Chen, Y. D.; Wang, H.; Li, Z.; Zheng, K.; Li, S.; Li, G. Transition-metal-mediated catalytic properties of CeO_2-supported gold clusters in aerobic alcohol oxidation. *Nano Res*., in press, https://doi.org/10.1007/s12274-017-1831-9.

[49] Liu, C.; Zhang, J.; Huang, J.; Zhang, C.; Hong, F.; Zhou, Y.; Li, G.; Haruta, M. Efficient aerobic oxidation of glucose to gluconic acid over activated carbon-supported gold clusters. *ChemSuSChem* **2017**, *10*, 1976–1980.

[50] Hayyan, M.; Hashim, M. A.; Al Nashef, I. M. Superoxide ion: Generation and chemical implications. *Chem. Rev*. **2016**, *116*, 3029−3085.

[51] Li, Y. Y.; Cheng, H.; Yao, T.; Sun, Z. H.; Yan, W. S.; Jiang, Y.; Xie, Y.; Sun, Y. F.; Huang, Y. Y.; Liu, S. J. et al. Hexane-driven icosahedral to cuboctahedral structure transformation of gold nanoclusters. *J. Am. Chem. Soc.* **2012**, *134*, 17997–18003.

[52] Chen, Y. D.; Zhang, C. L.; Yang, C. P.; Zhang, J. W.; Zheng, K.; Fang, Q. H.; Li, G. A Waugh type $[CoMo_9O_{32}]^{6-}$ cluster with atomically dispersed Co^{IV} originates from anderson type $[CoMo_6O_{24}]^{3-}$ for photocatalytic oxygen molecule activation. *Nanoscale* **2017**, *9*, 15332–15339.

[53] Kurashige, W.; Negishi, Y. Synthesis, stability, and photoluminescence properties of $PdAu_{10}(PPh_3)_8Cl_2$ clusters. *J. Clust. Sci.* **2012**, *23*, 365–374.

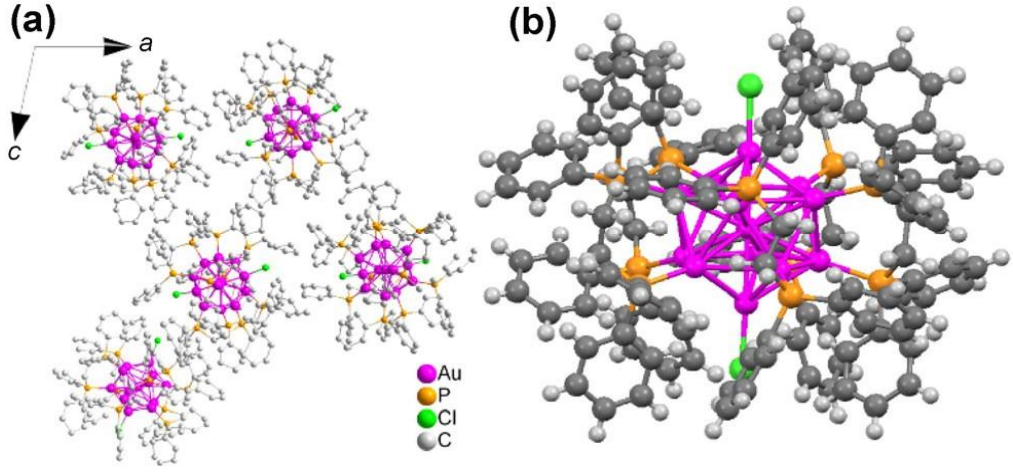

Figure 1 Full crystal structure of the $[Au_{13}(dppe)_5Cl_2]^{3+}$ cluster. (a) Five monomers are found in one unit cell. (b) Side view of a cluster monomer. Color code: Au, purple; P, orange; Cl, green; C, black; H, grey.

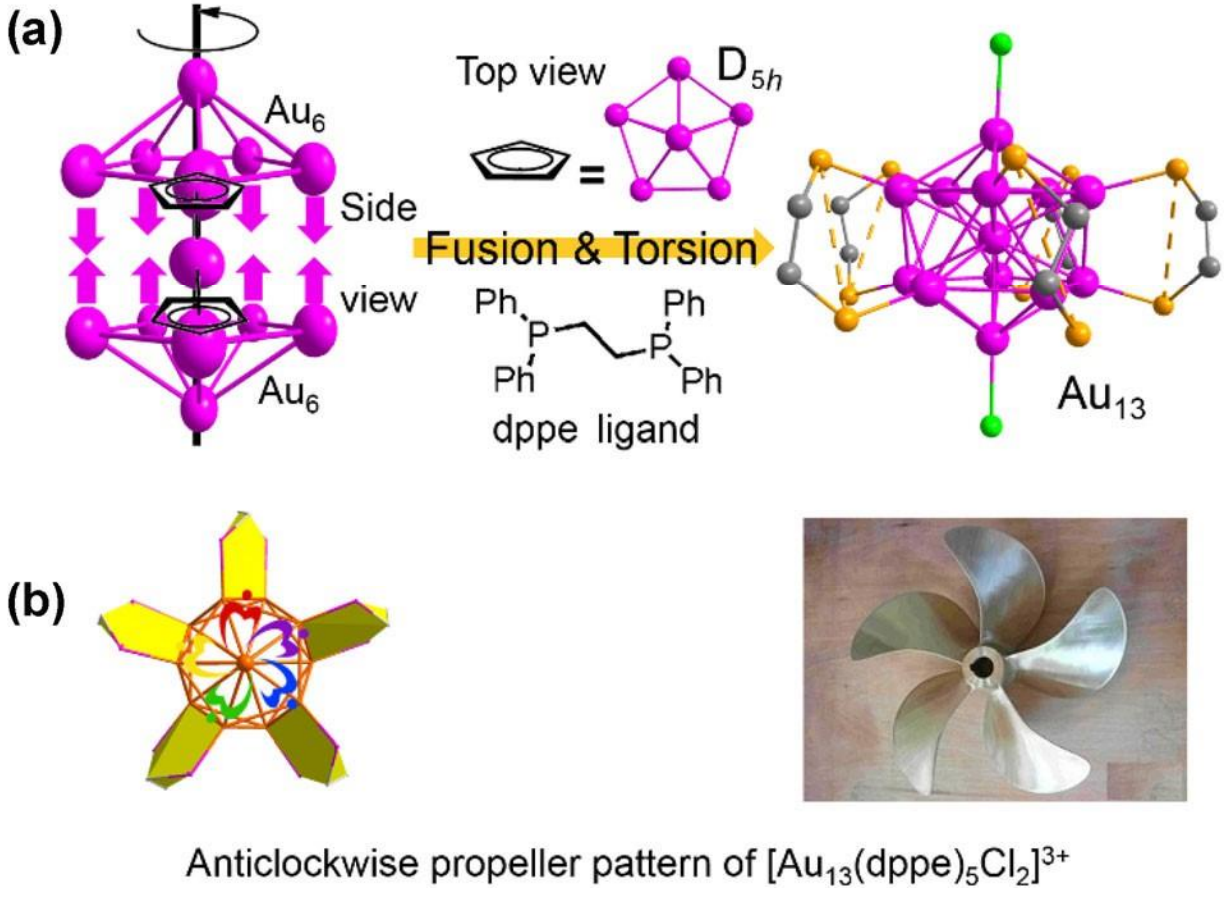

Figure 2 (a) Side view of the anatomy of the $[Au_{13}(dppe)_5Cl_2]^{3+}$ cluster. (b) Top view of the propeller arrangement of the Au_{13} cluster. Color code: Au, pink; P, orange; Cl, green; C, black. Phenyl groups are omitted for clarity.

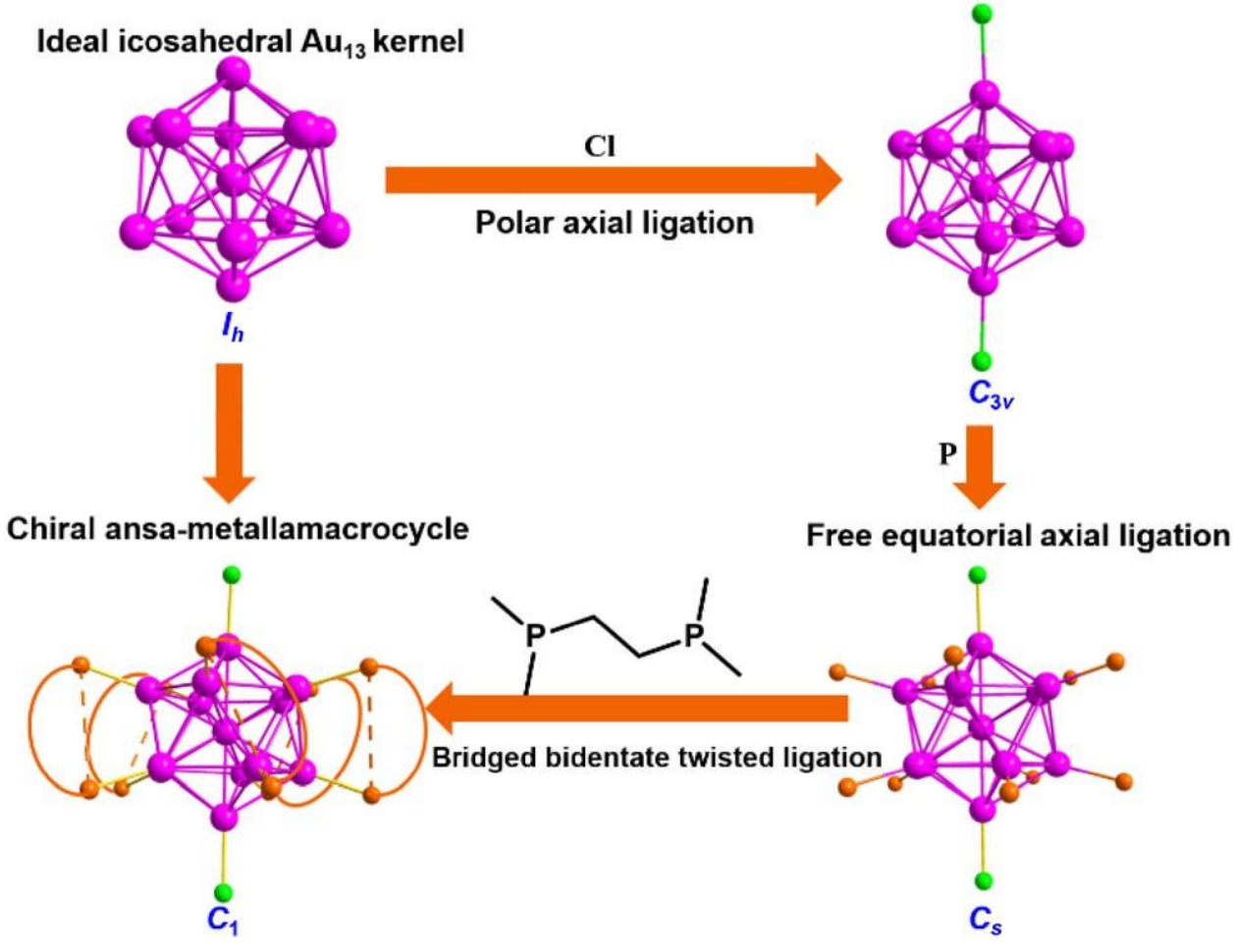

Figure 3 Intrinsic chirality generation of $[Au_{13}(dppe)_5Cl_2]^{3+}$ from symmetry reduction demonstration.

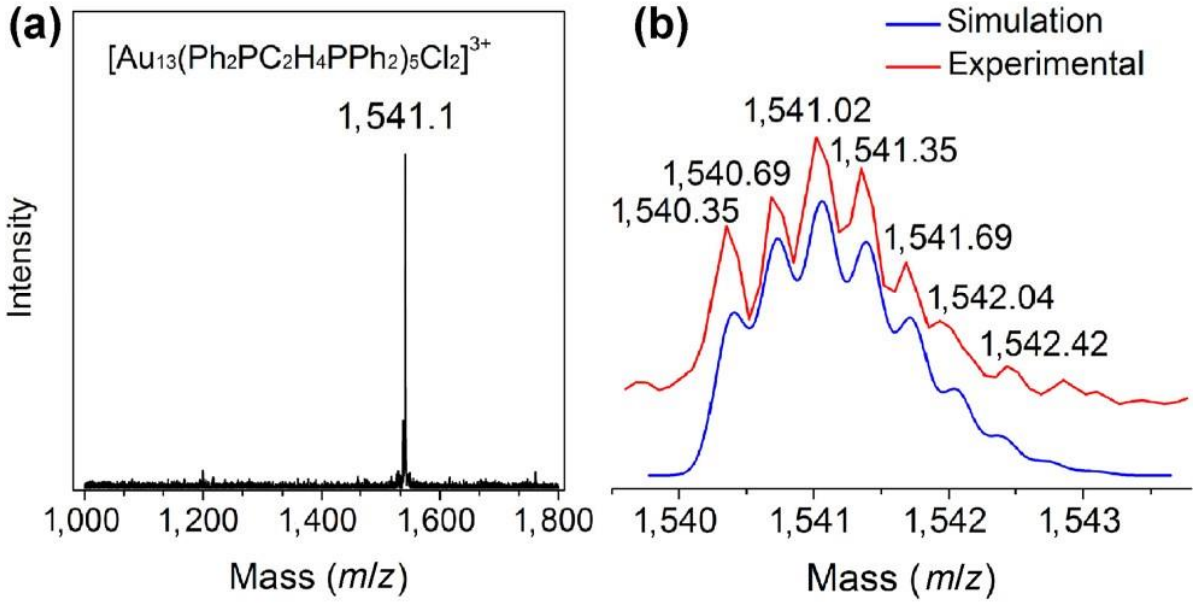

Figure 4 (a) ESI-TOF-MS analysis of the $[Au_{13}(dppe)_5Cl_2]^{3+}$ cluster and (b) experimental (red) and simulated (blue) isotopic patterns of the $[Au_{13}(dppe)_5Cl_2]^{3+}$ cluster.

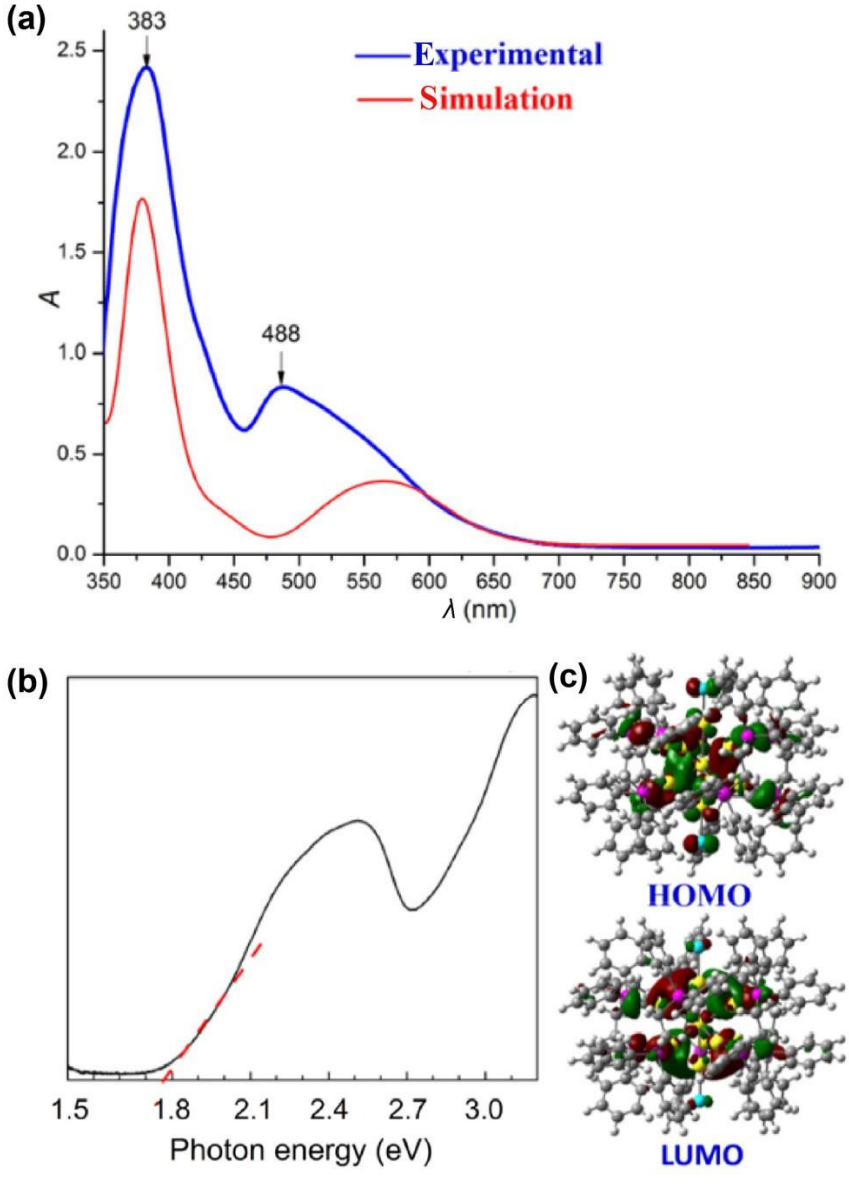

Figure 5 (a) Experimental (blue) and DFT simulated (red) UV/Vis spectra of the $[Au_{13}(dppe)_5Cl_2]^{3+}$ cluster. (b) Optical energy gap of the $[Au_{13}(dppe)_5Cl_2]^{3+}$ cluster. (c) HOMO and LOMO status of the cluster. at 132.96 eV (Fig. 6(a)). The nanocluster Au $4f_{7/2}$ binding energy (84.38 eV, Fig. 6(b)) was upshifted from Au foil by approximately 0.4 eV, but was 0.5 eV lower than that of the $Au(PPh_3)_2Cl$ complex [34]. These results indicated that the Au species were positively charged ($Au^{\delta+}$, where $0 < \delta < 1$).

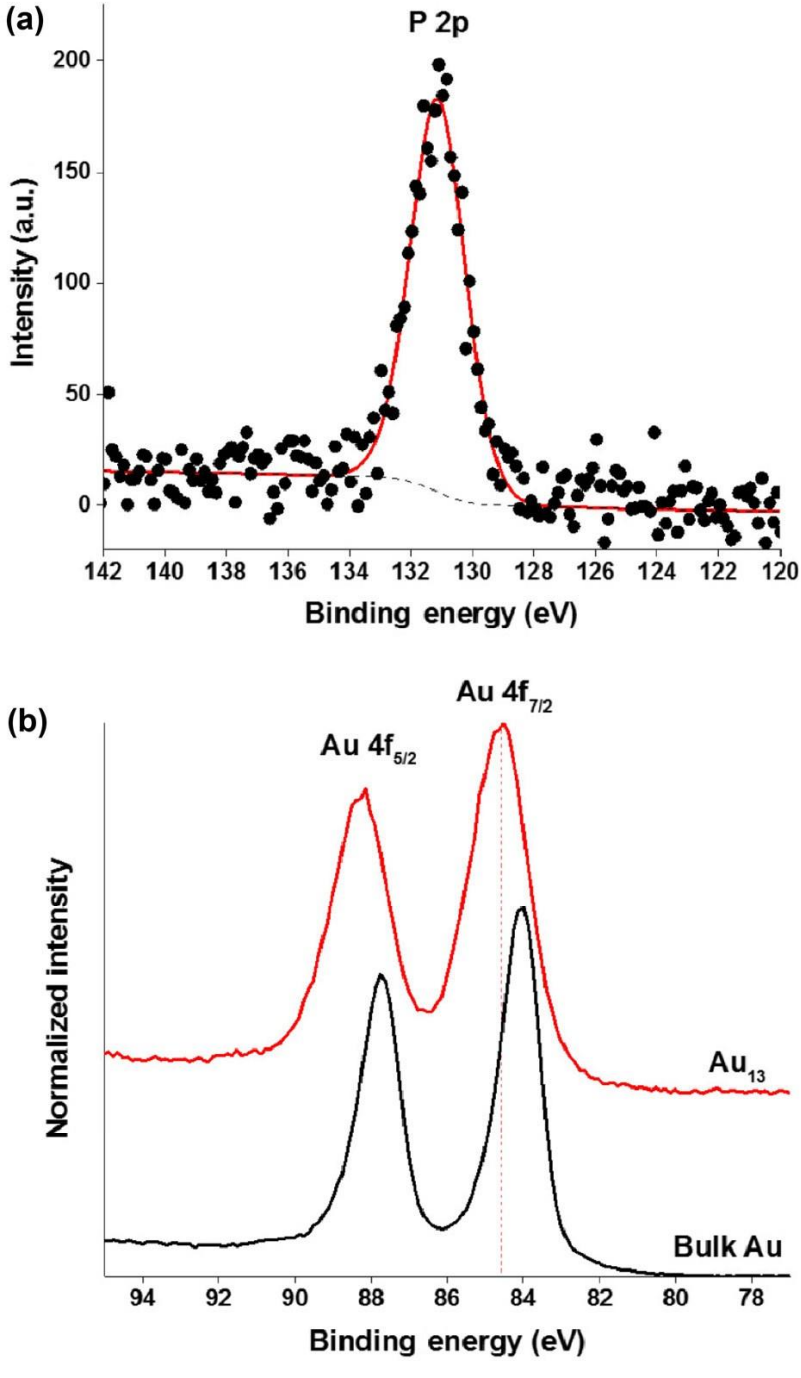

Figure 6 (a) P 2p spectral region of $[Au_{13}(dppe)_5Cl_2]^{3+}$ clusters and (b) Au 4f spectral region of $[Au_{13}(dppe)_5Cl_2]^{3+}$ clusters compared with bulk Au foil.

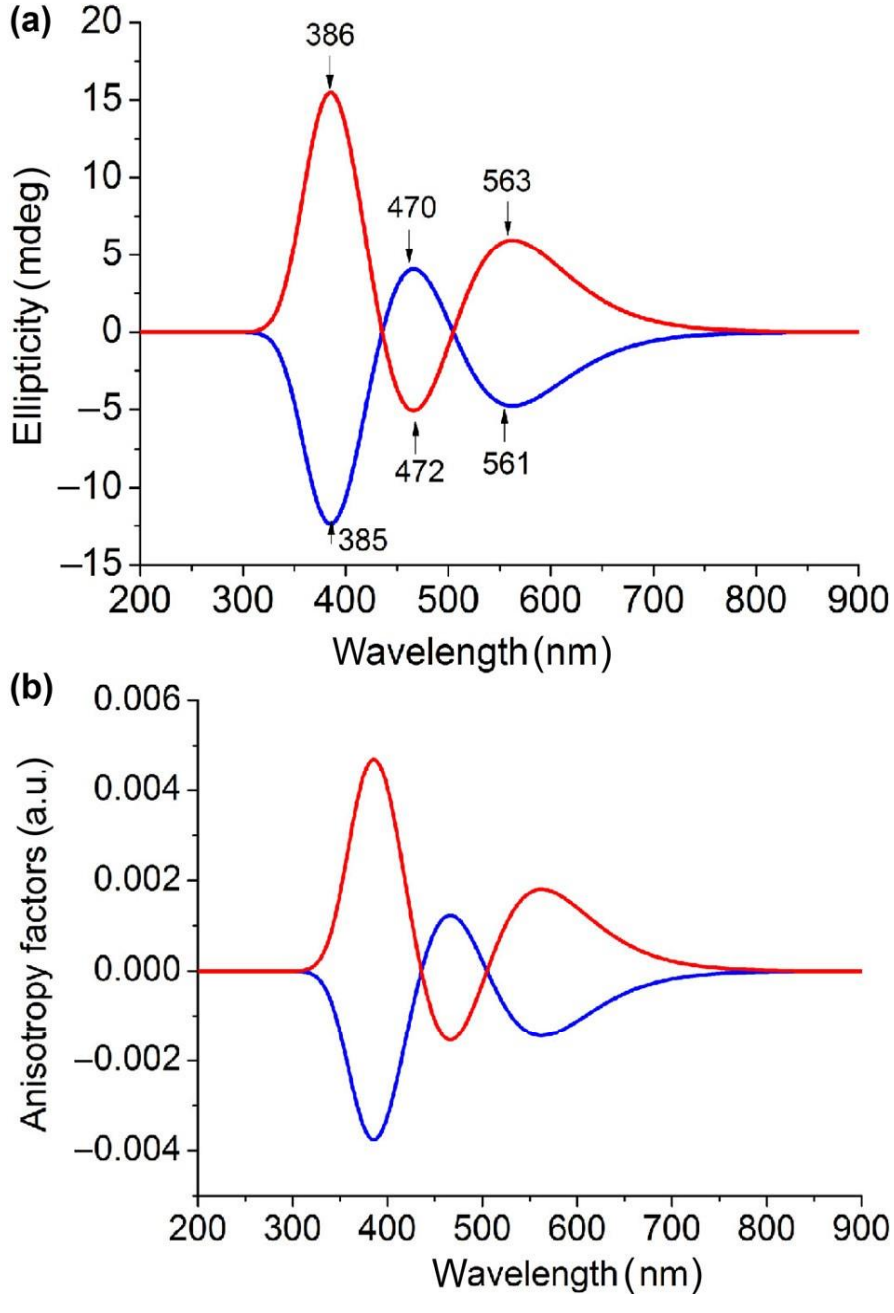

Figure 7 (a) ECD spectra of $[Au_{13}(dppe)_5Cl_2]^{3+}$ cluster enantiomers E1 (blue) and E2 (red) and (b) *g* factor of the $[Au_{13}(dppe)_5Cl_2]^{3+}$ cluster enantiomers.

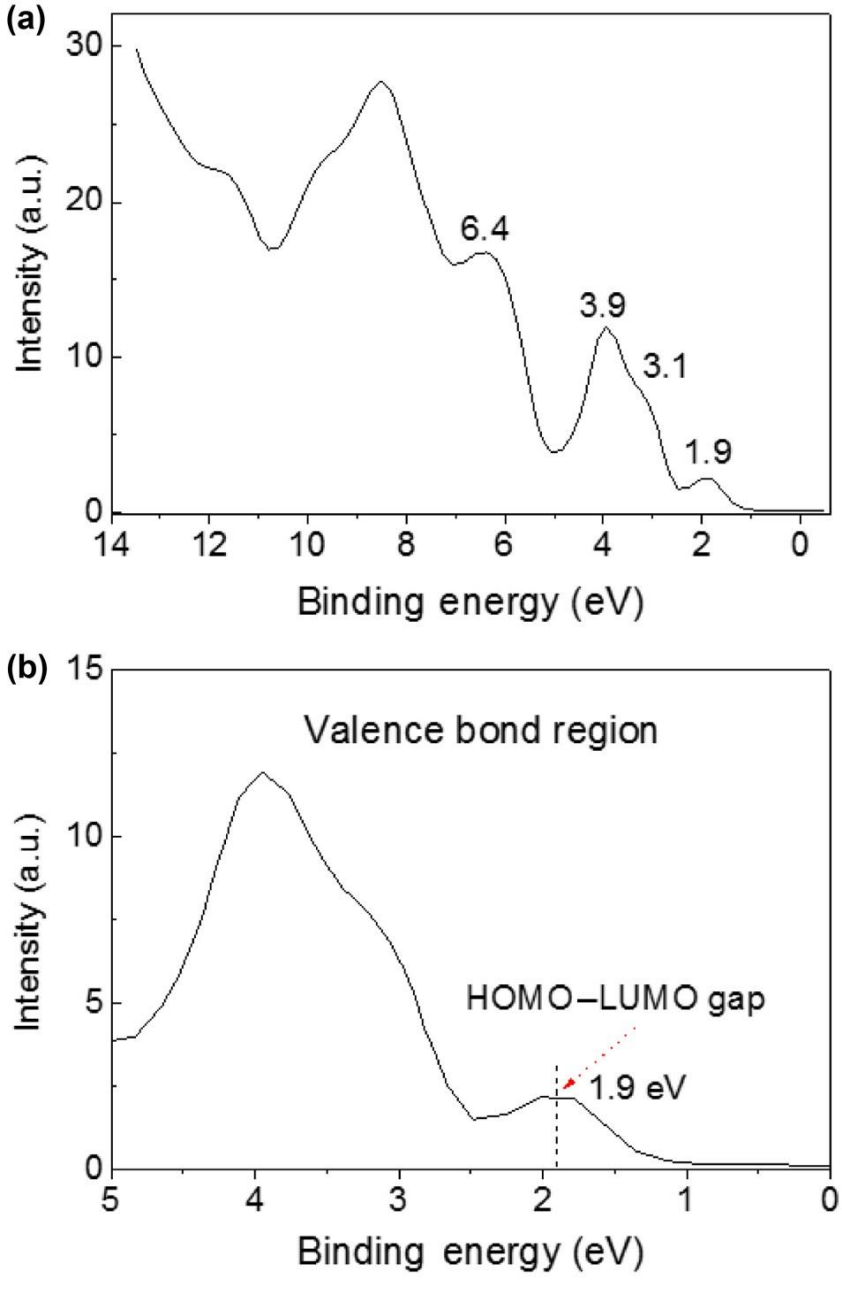

Figure 8 (a) UPS spectrum of $[Au_{13}(dppe)_5Cl_2]^{3+}$ nanocluster with (b) the valence band region. The HOMO−LUMO gap of the Au_{13} cluster was approx. 1.9 eV.

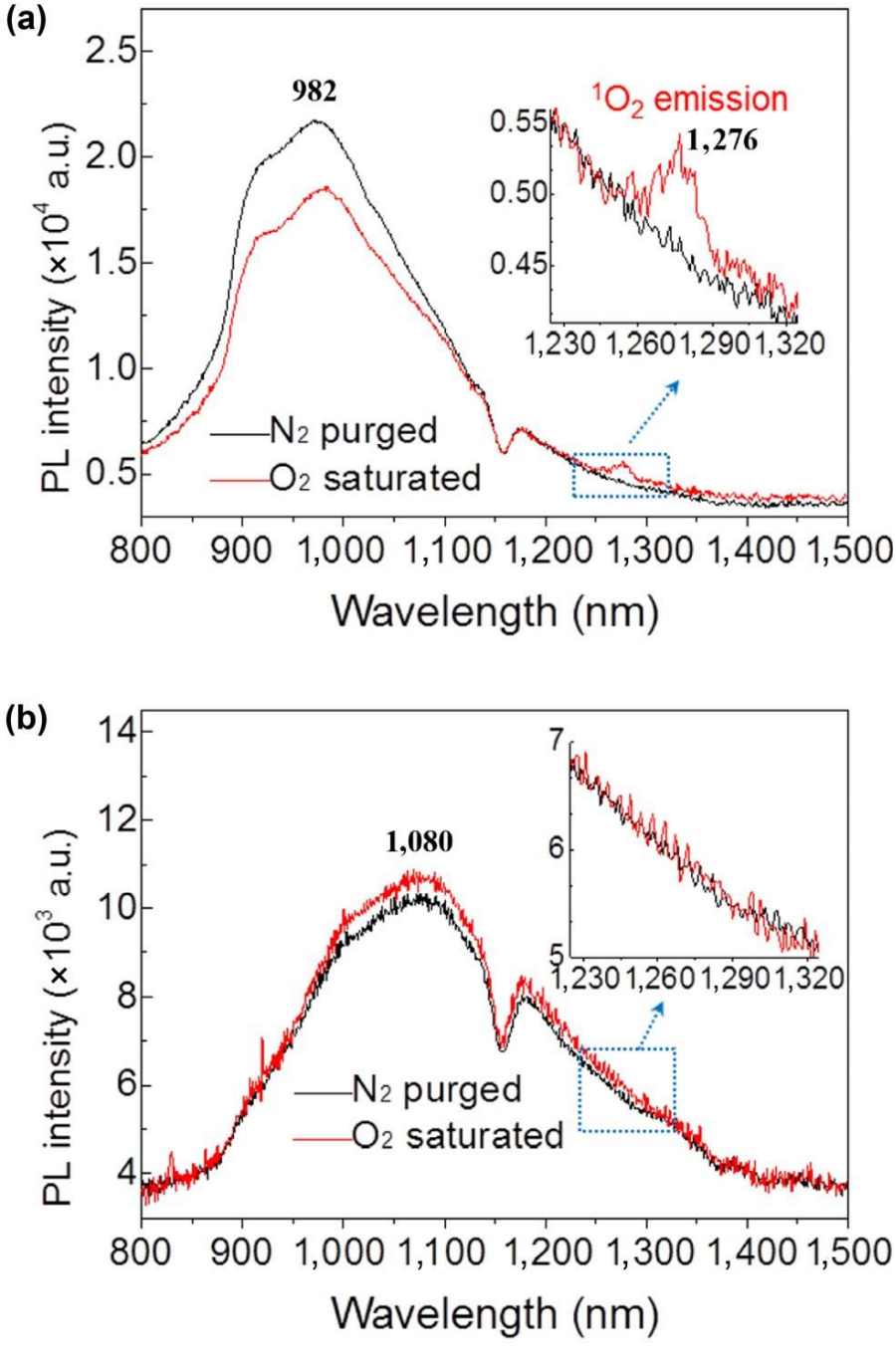

Figure 9 NIR PL spectra of (a) $Au_{13}(dppe)_5Cl_2$ and (b) $Au_{11}(PPh_3)_7Cl_3$ nanoclusters dissolved in N_2-purged or O_2-saturated CH_2Cl_2. Inset in (a): normalized PL spectra showing the $^3O_2 \rightarrow {}^1O_2$ transition.

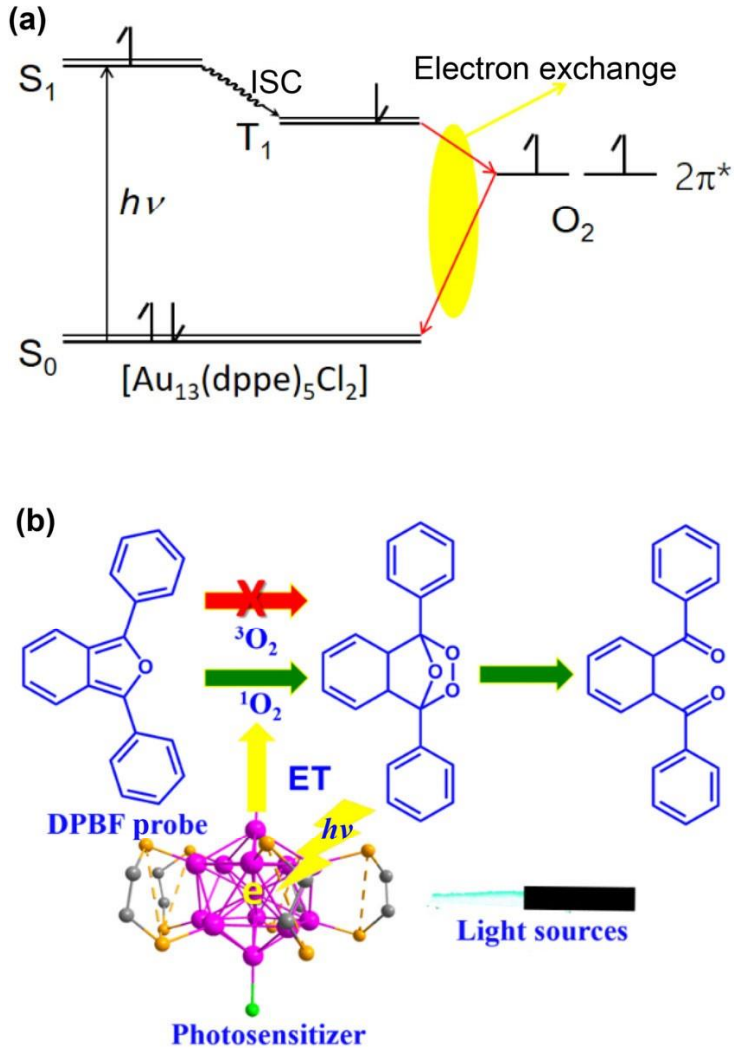

Figure 10 (a) Mechanism of Dexter-type electron exchange coupling between the Au_{13} cluster and $^3O_2$ for $^1O_2$ photogeneration. (b) Illustration of photooxidation of DPBF probe into 1,4-diphenyl-1,4,4a,8a-tetrahydro-1,4-epoxybenzo[d][1,2]dioxine by $^1O_2$ species.